Optomechanical Gyroscope Based on Micro-Hemispherical Shell and Optical Ring Resonators

Jamal N. A. Hassan [ID], *Graduate Student Member, IEEE*, Wenyi Huang, Maoyuan Wang [ID], Senyu Zhang, Guangjun Wen [ID], *Senior Member, IEEE*, and Yongjun Huang [ID], *Member, IEEE*

Abstract—Silicon photonic integrated circuits and micro-electro-mechanical systems enable the design of compact, high-performance micro-opto-electro-mechanical systems (MOEMS) gyroscopes, such as recently reported optomechanical gyroscopes. However, effective on-chip light coupling within a confined micro/nano system under vacuum posed challenges for conventional angular velocity measurements in prior optomechanical gyroscopes. Additionally, A core challenge in resonant gyroscopes is directly measuring resonant frequency displacement, necessitating alternative angular velocity detection techniques. Alternatively, this work presents the design of a novel optomechanical gyroscope based on the micro-hemispherical shell resonator integrated with optical ring cavity resonators. This integrated optomechanical device combines the principles of shell resonators and optical ring cavity resonators to enhance gyroscope performance. The high-Q optical ring resonators coupled via evanescent fields from the on-chip silicon waveguide, serve as the basic building block. Overall, the gyroscope design utilizes principles of both mechanical resonators and integrated photonics to address challenges in on-chip light coupling and angular velocity detection for next-generation optomechanical inertial sensors. Numerical simulations demonstrated the optomechanical micro-hemispherical shell resonator gyroscope could attain a calculated scale factor of 77.9 mV/(°/s) and total angle random walk of 0.0662 °/h$^{1/2}$ for a micro-hemispherical shell mass of 212 ng at an input laser power of 5 mW. These performance metrics suggest the proposed integrated optomechanical gyroscope design holds promise for applications requiring chip-scale inertial navigation, attitude measurement, and stabilization.

I. INTRODUCTION

GYROSCOPES have proven to be versatile inertial measurement tools, enabling angular motion sensing across a diverse array of application domains requiring precise orientation determination capabilities. As a rotational motion sensor, the gyroscope effectively quantifies angular velocity and is thus heavily relied upon for rotational dynamics monitoring in numerous industries [1]. Considerable research efforts have yielded numerous gyroscopic transducer designs aimed at precision angular motion sensing applications over recent decades. Upon examining the current state-of-the-art in solid-state gyroscopic technologies, three primary categories emerge for high-accuracy inertial measurement: hemispherical resonator gyroscopes (HRG), ring laser gyroscopes, and fiber optic gyroscopes [2], [3], [4]. Through continued optimization of resonant mode coupling, excitation transduction, detection schemes, and miniaturization of hemispherical shell fabrication, HRG technology has demonstrated maturity sufficient to achieve inertial-level angular motion sensing precision on par with high-end tactical and navigational grade inertial measurement units [5], [6]. Driven by the needs for high-precision inertial sensors with improved scalability, exhaustive research efforts have sought to miniaturize HRG for chip-scale implementations. In the nascent research on micro hemispherical shell resonator gyroscopes (MHSRG), early efforts focused on investigating alternative resonator geometries and fabrication methodologies capable of retaining high Q-factors despite miniaturization [7], [8], [9], [10], [11], [12], [13]. Concurrently, the field has seen notable advancements in transduction mechanisms for MHSRG resonators, with structural detection electrode configurations undergoing rigorous investigation to enhance sensing capabilities [11]. However, unavoidable nanoscale variations introduced during the fabrication of these micro-resonating gyroscopic elements have been shown to induce undesirable phenomena such as resonant frequency splitting, modal deformations, and asymmetric damping effects [12], [13], [14]. Additionally, measurement stability and accuracy attainable with conventional MHSRG paradigms relying on capacitive detectable schemes

have been limited by inherent sensitivity to electromagnetic interference and thermomechanical perturbations introduced by ambient thermal vibrations.

The field of micro-opto-electro-mechanical systems (MOEMS) incorporating integrated photonic elements has seen considerable maturation in gyroscopic implementations facilitated by advancing nanomanufacturing protocols for optical devices [15], [16], [17]. Notably, the domain of cavity optomechanics, wherein optical and mechanical resonators are strongly coupled within an integrated photonic system, has witnessed considerable progression that positions it as a highly promising transduction paradigm for photonic sensors [18], [19]. Representative optomechanical system configurations that have shown promise within this domain include optical ring resonators harnessing circulating light in micron-scale rings as well as whispering gallery mode (WGM) cavities [17], [20]. Extensive scholarly inquiry has explored the viability and immense prospective capabilities of optomechanical gyroscope paradigms [21], [22], [23], [24], [25], [26], [27], [28]. While past scholarly works have extensively explored the viability and prospective capabilities of optomechanical gyroscope schemes through theoretical modeling and feasibility analysis, empirical substantiation of functional optomechanical gyroscope designs remains an outstanding challenge.

This work presents the design of a novel optomechanical gyroscope based on a micro-hemispherical shell resonator integrated with optical ring cavity resonators. The main contributions from our design are summarized as follows:

- Novel optomechanical micro-gyroscope design: The device combines the principles of shell resonators and optical ring cavity resonators to enhance the performance of gyroscopes.
- Solution for measuring resonant frequency displacement: The device uses multi-ring optical cavities as sensing elements in angular vibration sensors, which can detect the displacement of the resonant frequency indirectly.
- Advantages of the integrated device: The device offers a compact and robust mechanical structure, improved sensitivity and precision in measuring angular velocity, and accurate measurements of angular velocity using resonant waves.

This paper is organized as follows: Section II presents the operating principle of the optomechanical micro hemispherical shell gyroscope (OMHSRG), and Section III shows the performance characterization of optomechanical MHSRG integrated with the optical ring resonator. Section IV presents the comparative study. Finally, Section V presents the conclusions.

II. OPERATING PRINCIPLE

A. The Architecture and Operational Concepts of the Optomechanical Micro Hemispherical Shell Gyroscope (OMHSRG)

The electrostatic actuation and released mechanical parts inherited from nano-electro-mechanical systems were combined with silicon photonics features such as on-chip light coupling and fiber packaging for vacuum and cryogenic operation [29].

Firstly, the micro-resonator was designed from boron-doped polysilicon as a hemispherical shell geometry. The hemispherical shell resonator, has a symmetrical capacitive design with dimensions on the micrometer scales [19], [30], [31], [32], [33]. The boron-doped polysilicon is both an electrical and optical conduction element in designing a hemispherical shell resonator. A hemispherical shell resonator consists of a thin film of polysilicon deposited on a boron-doped polysilicon cylindrical substrate and etched into a hemispherical shape. By doping the polysilicon film with boron, the electrical and optical properties of the resonator can be tuned and optimized. For example, a heavily boron-doped polysilicon film can increase the conductivity and reduce the resistivity of the resonator, improving its electrical performance and reducing its power consumption. A lightly boron-doped polysilicon film can reduce the band gap and increase the absorption of the resonator, improving its optical performance and increasing its sensitivity. The micro-shell resonator has a diameter of approximately 75 μm and a thickness of 1 μm for the shell. It is anchored to the cylindrical substrate at the center, which acts as an element of connection between the electrodes and the base substrate (lower layer). Four metallic layers are employed on the boron-doped poly-silicon electrodes to establish outer connections. These electrodes encompassing the hemispherical resonator at angular positions of 0°, 90°, 180°, and 270° are utilized to induce the primary resonant mode, specifically the first wineglass mode deformation (primary resonant mode). Concurrently, we designed an optomechanical system utilizing four optical ring resonators evenly distributed around the hemisphere of a central mechanical resonator to enable strong optomechanical coupling within a reduced modal volume positioned at 45°, 135°, 225°, and 315° to detect the second wineglass mode deformation (secondary resonant mode), thereby enabling sensing. The micro-ring resonators are oriented to be aligned with the periodic hemispherical shell nanostructure of the mechanical element. Light from a tunable diode laser is coupled in and out of the waveguide via two grating couplers with a coupling efficiency of 10% each. This configuration allows for optomechanical interactions between the co-localized optical and mechanical modes owing to the Maxwell stress tensor generated by the circulating optical fields in the high-Q micro-ring resonators and the mechanical oscillations of the micro-shell on the optical ring resonator. Fig. 1(a) shows the micro-resonator gyroscope design. Fig. 1(b) illustrates the schematic of the optical ring and waveguide optomechanical system and its measurement principle.

Secondly, the operating mechanism of the optomechanical micro hemispherical shell resonator gyroscope is based on the interaction between a hemispherical shell resonator and an optical ring resonator, which exploits the enhanced light-matter coupling in a high-Q optical cavity and a high-Q mechanical resonator [14], [19]. The shell resonator is driven by electrostatic actuation to vibrate in a wineglass mode. According to finite element modal analysis, Fig. 1(c) depicts the mechanical wineglass deformation modes of the micro-shell resonator system as a driving system. Fig. 1(d) illustrates the modal structure of the optomechanical hybrid optical ring resonator, which is interfaced with a waveguide. The waveguide facilitates the propagation of
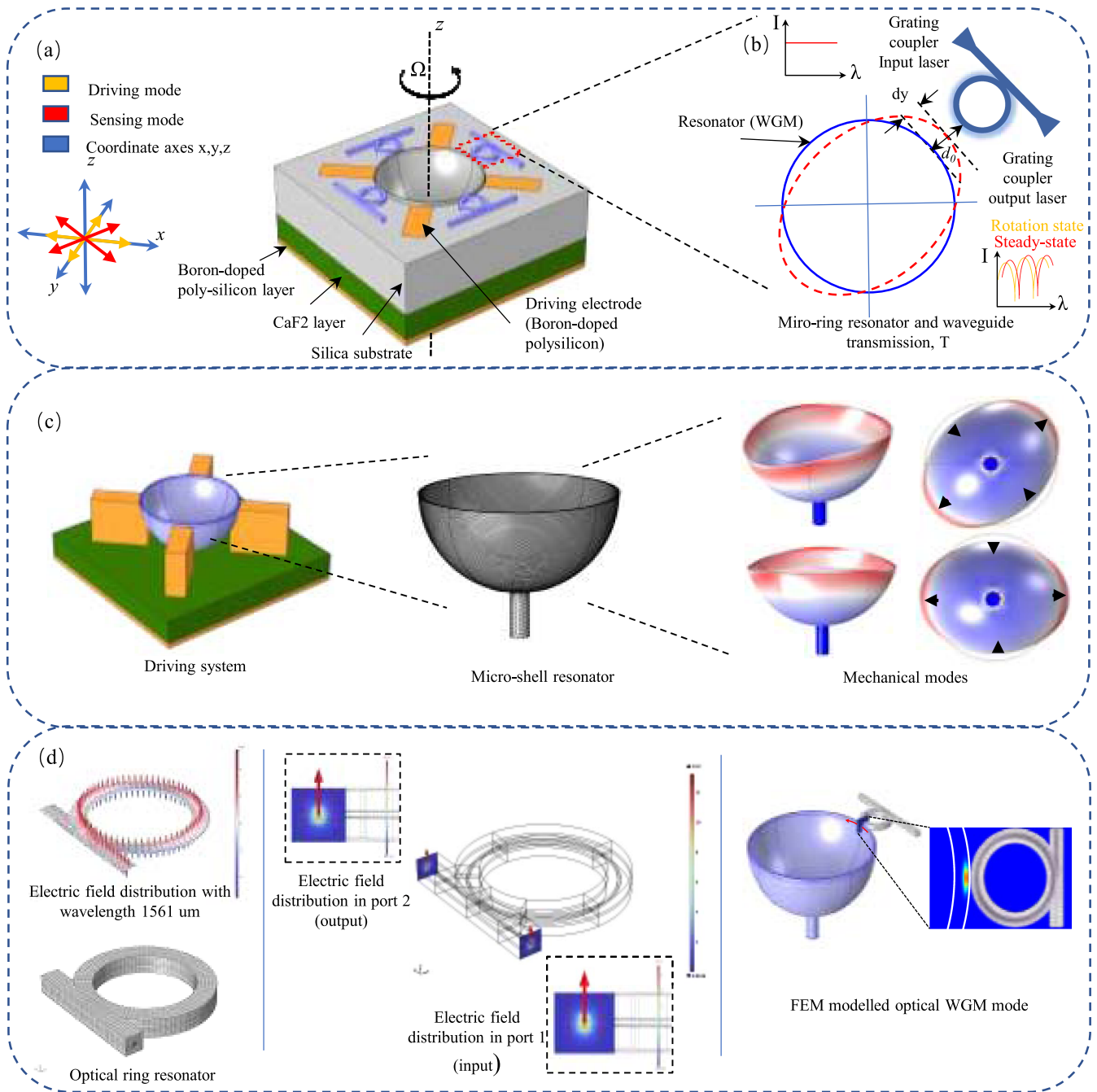
Fig. 1. (a) and (b) Three-dimensional representation and functional mechanism of the optomechanical micro-shell resonant gyroscope (OMSRG), (c) driving mechanism and finite element method (FEM) modeled mechanical deformation modes of the wineglass structure in the micro-scale resonant gyroscope, and (d) finite element method (FEM) modeled optical whispering gallery mode (WGM).

laser input via out-coupling mechanisms with the waveguide gratings, as demonstrated in Fig. 2(a). When the device rotates, the Coriolis force causes a displacement of the shell resonator, which causes the driving and sensing mechanical modes to be separated by 45 degrees, which modulates the optical resonance frequency and power of the optical ring resonator, altering the optical frequency within the waveguide detectable by the photodetector relative to a reference frequency ω_d. A photodetector detects the output power and converts it to an electrical signal proportional to the rotation rate.

Thirdly, the behavior of the optical ring resonator and its advantages in the sensing mechanism are determined by several optomechanical coupling parameters, such as the extrinsic coupling rate, the scattering loss, the external test mass coupling rate, and the laser-cavity detuning. These parameters depend on the coupling distance between the shell resonator and the ring resonator, which affects the evanescent field intensity and the effective refractive index. The device can achieve high sensitivity and precision in measuring angular velocity by controlling the coupling distance and tuning the laser wavelength. The
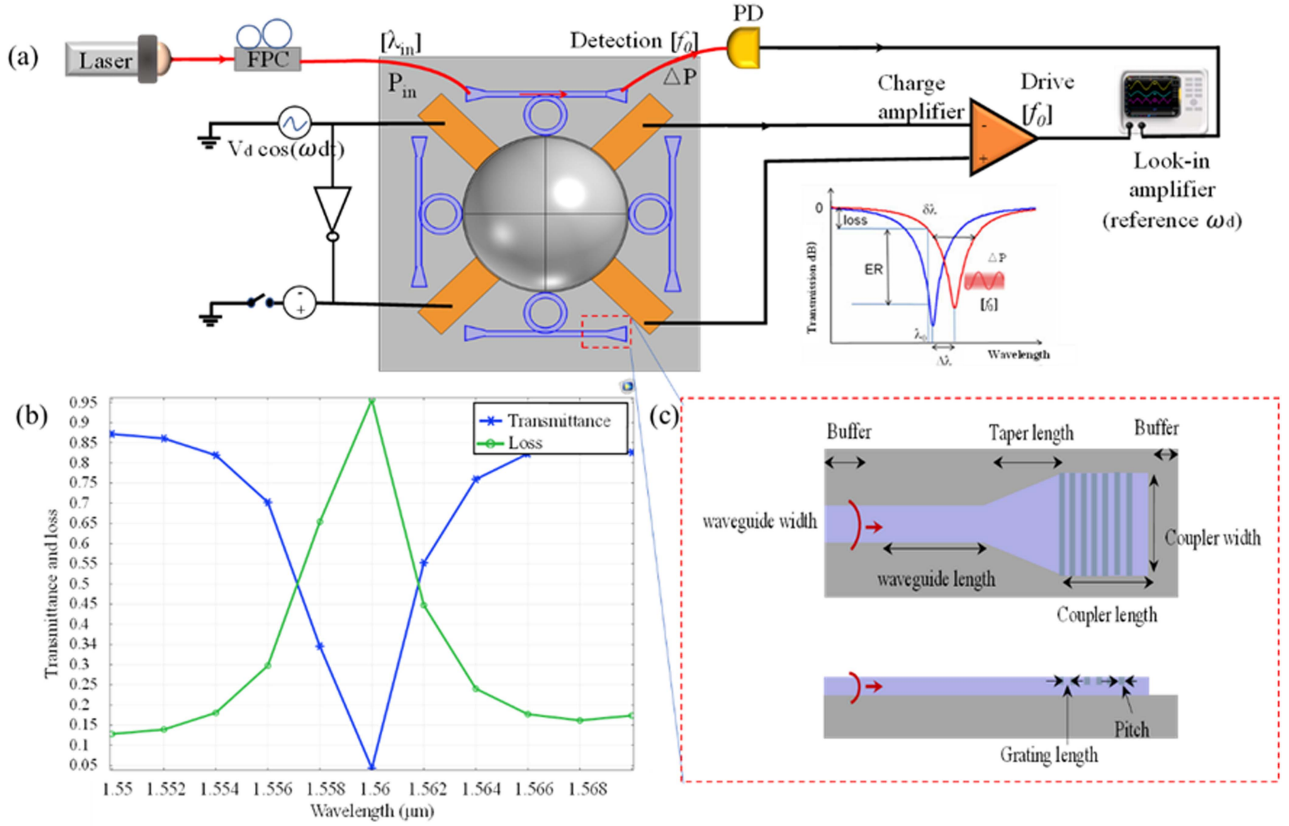
Fig. 2. (a) Optomechanical readout scheme. FPC stands for fiber-polarization controller, PD for photodetector, and LIA for lock-in amplifier. Red and dark lines are optical and electrical signals, respectively. The optical ring resonator vibrating at frequency f_0 modulates the resonance wavelength of the optical cavity and consequently the light output power at f_0, (b) resonance wavelength corresponding to transmission below 0.05, and (c) schematic structure for a 1D grating coupler (GC) with linear waveguide taper.
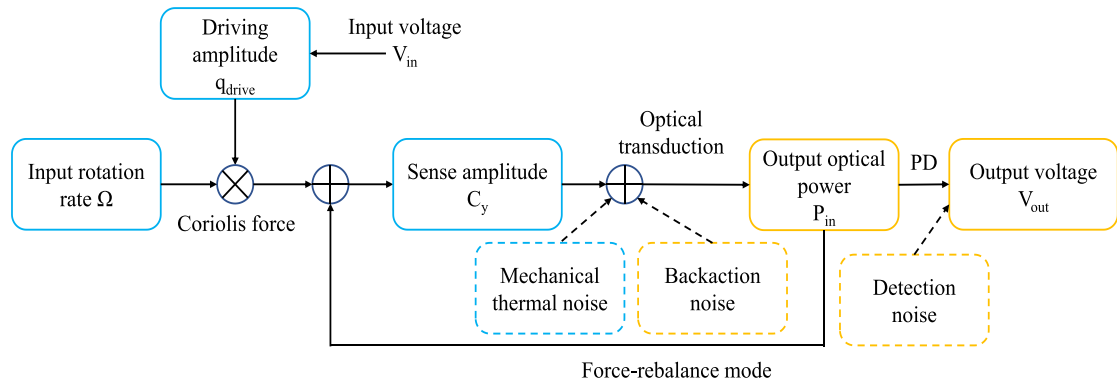

Fig. 3. The general operational scheme for the planned optomechanical OMHSRG.

optical ring resonator also provides high optical quality factors and small mode volumes, desirable for applications requiring chip-scale inertial navigation, attitude measurement, and stabilization. The characteristics of the optical ring resonator are as shown in Fig. 2(b), the Transmission and loss of the micro-ring resonator, and Fig. 2(c) Schematic structure for a 1D grating coupler (GC) with linear waveguide taper. Fig. 3 summarizes the overall operating-system.

Lately, they have just begun producing mm-scale HRG to improve their operational frequency for high-speed projectiles

[14], [34], [29]. The fabrication process of an optomechanical micro hemispherical shell gyroscope begins with Electrical Discharge Machining (EDM) to create a rough hemispherical shape on a lithium niobate wafer, which is then refined with a second EDM process. The surface is then smoothed and polished using HNA Chemical Polishing. Reactive Ion Etching (RIE) is used to etch the electrodes, which are then filled with boron-doped polysilicon. A Low-Temperature Oxide (LTO) layer is deposited on the hemispherical surface as a sacrificial layer. A boron-doped polysilicon layer is then deposited on

top of the LTO layer to form the final hemispherical shell. A Plasma-Enhanced Tetraethyl Orthosilicate (PE-TEOS) layer is deposited on the boron-doped polysilicon layer to serve as a hard mask for the subsequent boron-doped polysilicon dry etching step. The PE-TEOS layer is then polished using a Chemical Mechanical Polishing (CMP) process. The boron-doped polysilicon layer is etched using the PE-TEOS layer as a mask using a Reactive Ion Etching process. Finally, a backside lithography and etching process is performed to create an anchor hole on the backside of the wafer, allowing the hemispherical shell to be attached to the base substrate. The goal of this process is to produce high-quality hemispherical structures for use in high-speed projectiles. The fabrication should be done using the VLSI process in a clean room of industrial quality. The biggest challenge is co-fabricating the optical ring and optical coupling waveguide with the optomechanical MHSRG due to differing nano-fabrication techniques and requirements.

The other steps show the fabrication process of an optical ring resonator with a waveguide and a grating coupler on the LNOI platform. The process begins with the deposition of a thin layer of SiO2 on the LNOI wafer using Plasma-enhanced chemical vapor deposition (PECVD), which serves as a hard mask for Ar+ ion milling. A layer of positive photoresist (PR) is then spin-coated on the SiO2 layer and patterned by photolithography to define the waveguide and the grating coupler. The SiO2 layer is etched by reactive ion etching using the PR as a mask, after which the PR is removed by acetone. The LNOI layer is etched by Ar+ ion milling using the SiO2 layer as a mask, and then the SiO2 layer is removed by buffered oxide etch (BOE). A layer of negative PR is spin-coated on the LNOI layer and patterned by photolithography to define the optical ring resonator. The LNOI layer is etched by Polishing-Like Atomically Controlled Etching (PLACE) using the PR as a mask, and then the PR is removed by acetone. PLACE consists of three steps: chemical etching by HF solution, mechanical polishing by a polishing pad, and rinsing by deionized water. These steps are repeated until the desired etching depth is reached. The final device, comprising an optical ring resonator coupled with a waveguide and a grating coupler for light input and output, is obtained after BOE removes the residual SiO2 layer.

B. Analysis of the Driving Mechanism in Optomechanical Micro Hemispherical Shell Resonator Gyroscope

The gyroscope design can benefit from a compact and robust mechanical construction by adopting a hemispherical shell resonator, assuring stability and longevity [35]. The proposed OMHSRG first needs to be driven by Out-of-plan electrodes. By positioning the actuator electrodes at the modal amplitude antinodes, the resonant motion's driven amplitude can be excited and regulated via electrostatic actuation. This results in a stable vibration of the hemispherical shell in the first wineglass mode (depicted as the primary motion mode in Fig. 4(a)), which corresponds to the n = 2 mode utilized for gyroscopic sensing. According to the Kirchhoff-Love hypothesis, and the thin shell theory of elasticity, the shell fulfills the geometric equation of the deformation component and displacement, the elastic relation
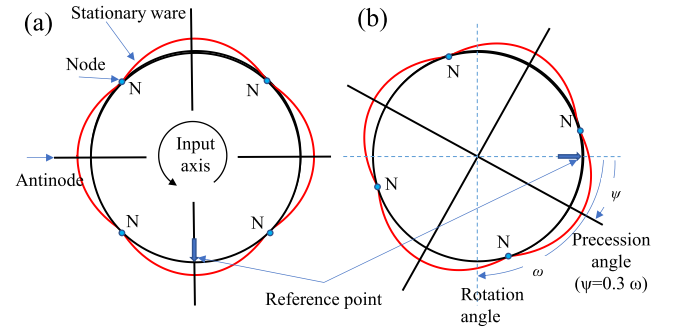

Fig. 4. Angle hysteresis principle of the hemispherical resonator (a) the mode deformation of the first wineglass mode (primary motion mode), (b) a slight vibrating moment in the detection mode (secondary motion mode).

equation, and the force balance equation [36]. The differential equation for the center surface area of the hemispherical shell is created by combining three equations, as a mention in Appendix A. A differential equation can be solved to determine the displacement field distribution or force field distribution near the shell for a specific boundary condition. The dynamics of the mass under a constant angular rate Ωz along the z-axis and harmonic excitations along the x and y-axes are governed by a system of two coupled differential equations.

$$M\frac{d^2x}{dt^2} - 2M\Omega_z\frac{dy}{dt} + c\frac{dx}{dt} + kx = F_x \tag{1}$$

$$M\frac{d^2y}{dt^2} - 2M\Omega_z\frac{dx}{dt} + c\frac{dy}{dt} + ky = F_y \tag{2}$$

Considering a basic hemispherical resonator gyroscope (HRG) model with two vibration modes (X and Y). The resonant frequencies of X and Y are the same as those described by $\omega = \sqrt{k/M}$. Let x and y denote the generalized coordinates corresponding to these two modes, with M representing the proof mass and k the spring constant, which is equal for both modes. F_x and F_y denote the artificial forces applied to the HRG by four electrodes, as shown in Fig. 5(a), and the capacitance gap between the electrostatic electrode and hemispherical shell resonator, as a shown in Fig. 5(b). In this model, damping terms and cross-coupling terms between the two modes are neglected. Equations (1) and (2) describes the linear motion along the X and Y axes excited by electrostatics, assuming Ω_z equals zero [37], [38]. The exterior actuator electrode plates have a spherical fan-shaped form, as shown in Fig. 5(c). The θ_{ab} and θ_{at} are the latitude range of electrodes. φ_{al} and φ_{ar} are the longitude ranges of the electrodes.

The driving force, with a constant frequency ω and a constant amplitude F_0, is applied solely along the x-axis. The resonator displacements in both coordinate axes, under steady-state conditions, are harmonic signals with the same frequency as the driving force.

$$x = x_0e^{j(\omega t+\theta_x)}, y = y_0e^{j(\omega t+\theta_y)} \tag{3}$$

Assuming that $F_x = F_0e^{j\omega t}$ and $F_y = 0$, where F_0, x_0, and y_0 are real constants, the complex amplitudes of each axis can be
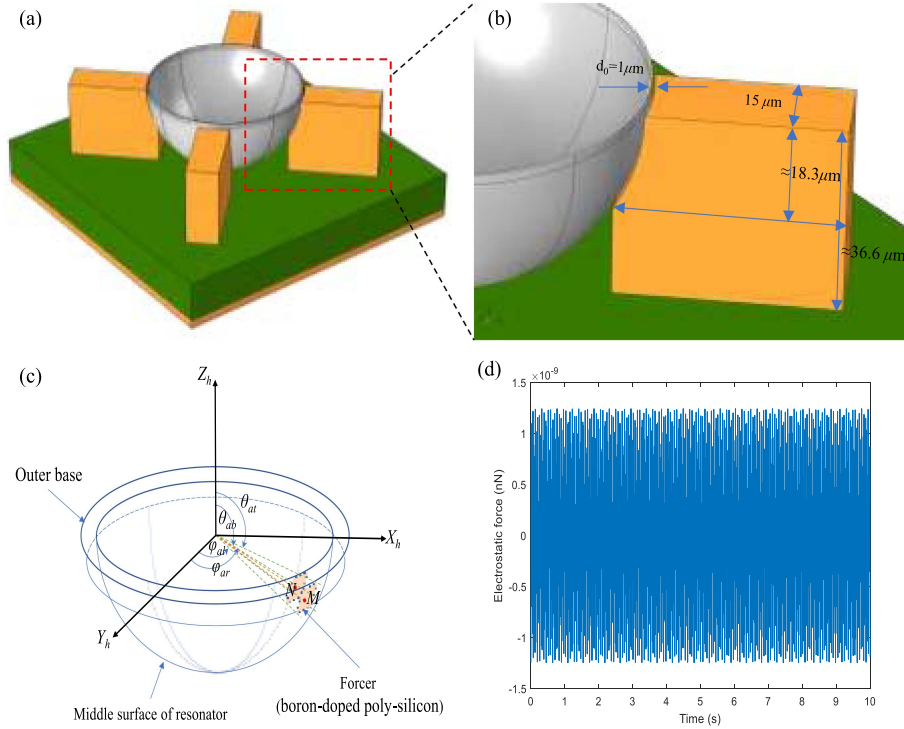
Fig. 5.　(a) The structure diagram of the four electrodes of the driving system, (b) the structure diagram shows the capacitance gap between the electrostatic electrode and hemispherical shell resonator, (c) the structure diagram of actuator electrodes, and (d) depicting the temporal fluctuation of electrostatic force.

obtained by substituting (3) into (1) and (2) and performing some algebraic operations.

$$x_0 e^{j\theta_x} = \frac{-M\omega^2 + jc\omega + k}{(-M\omega^2 + jc\omega + k)^2 - 4M^2\Omega_z^2\omega^2} F_0 \quad (4)$$

$$y_0 e^{j\theta_y} = \frac{j2\Omega_z\omega}{(-M\omega^2 + jc\omega + k)^2 - 4M^2\Omega_z^2\omega^2} F_0 \quad (5)$$

Deriving the ratio of (5) to (4), we obtain the relation of

$$\frac{y}{x} = \frac{y_0}{x_0} e^{j(\theta_y-\theta_x)} \equiv R_0 e^{j\theta} = \frac{-j2M\omega}{-M\omega^2 + jc\omega + k}\Omega_z \equiv A\Omega_z \quad (6)$$

The complex ratio of the vibration amplitudes along the two coordinate axes is linearly dependent on the angular rate Ω_z, irrespective of the driving force magnitude. The slope of this dependence, A, is a complex constant that only depends on the resonator characteristics. Therefore, by knowing the resonator parameters a priori, the angular rate Ω_z can be determined from the measurements of the complex amplitudes. Equation (6) implies that the complex ratio y/x is a linear function of the complex constant A in the complex plane. In the case of a symmetric resonator, this function intersects the origin and has a zero magnitude, $R_0 = 0$, when the angular rate Ω_z is zero. The complex constant A, which represents the resonator properties, can be determined experimentally by measuring the ratio y/x for at least two known values of Ω_z.

The actuator electrodes employed for exciting the desired vibrational modes are driven by an alternating current voltage source operating at a frequency equivalent to half the second-order resonant mode's natural frequency, as mathematically described in (7) [37].

$$V(\theta,\varphi,t) = \begin{cases} 0 & other \\ V_0 \cos\left(\frac{\omega_2 t}{2} + \frac{\varphi_{al}+\varphi_{ar}}{2}\right) & \begin{matrix} \theta_{at} \leq \theta \leq \theta_{ab} \\ \varphi_{al} \leq \varphi \leq \varphi_{ar} \end{matrix} \end{cases} \quad (7)$$

Given the nanoscale dimensions of the device, the capacitive gap formed between the actuator electrodes and resonating shell is considerably smaller than the hemispherical shell's radius. As such, the actuator electrodes may reasonably be approximated as parallel plate capacitors for analytical modeling purposes. Under this assumption, the mild curvature of the hemispherical boundaries can be neglected, simplifying the capacitance formulation. The dominant electrostatic interaction force arising from the actuator electric field and acting upon the vibrating shell structure is then described by (8) [39].

$$F_{drive} = \begin{cases} -\frac{\varepsilon_0 V_0^2}{2d^2}\cos^2\left(\frac{\omega_2 t}{2} + \frac{\varphi_{al}+\varphi_{ar}}{2}\right) & \begin{matrix} \theta_{at} \leq \theta \leq \theta_{ab} \\ \varphi_{al} \leq \varphi \leq \varphi_{ar} \end{matrix} \\ 0 & other \end{cases} \quad (8)$$

where V_0 represents the potential voltage applied between the parallel actuator electrode plates, ε_0 is the vacuum permittivity constant equal to 8.85×10^{-12} *F/m*, and d denotes the inter-plate separation comprising the capacitive gap, the calculation capacitance by $C = \varepsilon_0 A/d$. By omitting the DC bias term in the resultant electrostatic force expression, which does not

contribute to resonant modal excitations, (8) can be reduced to a simpler form focused only on the modulated AC driving force component.

$$F_{drive} = -\frac{\varepsilon_0 V_0^2}{4d^2} \cos(\omega_2 t + \varphi_{al} + \varphi_{ar}) \quad (9)$$

The normal vector to the resonating shell's outer surface corresponds to the direction of electrostatic force generated by the actuator electrodes [38]. However, as Coriolis forces induce tangential vibrational motion, the outer surface normal vector undergoes continual reorientation. This tangential deflection component arises due to small amplitude distortions superimposed upon the nominal spherical geometry due to modal vibrations. Though such deformations are minuscule in scale compared to the shell radius, they remain proportional to the transmission of resonant energy into sensing modes. Fig. 5(d) shows the temporal variation of the electrostatic force, calculated numerically from (9), as a function of time for a fixed input voltage of 5 mV and a gap distance of 1 μm between the electrode and the resonator.

C. Sensing Mechanisms in Optomechanical Micro Hemispherical Shell Resonator Gyroscope

The proposed micro hemispherical shell gyroscope design necessitates electrostatic actuation to reliably excite the target wine-glass vibrational mode. The strategic placement of actuator electrodes at the modal amplitude antinodes allows for the extension of their functionality to stimulate and maintain the driven amplitude of the resonant motion. This is achieved through the implementation of closed-loop control governed by mechanical equations, as detailed in Appendix B. This approach ensures a stable and controlled resonant motion. Based on the underlying Coriolis effect principle, subjecting the gyroscope body to an applied rotation rate Ω will induce a phase lag between the physical orientation of the resonant shell and its driven vibrational mode shape of approximately 0.3 times the total rotation angle [36]. This phase offset engenders a weak vibrating moment in the orthogonal detection axis mode (depicted as the secondary motion mode in Fig. 4(b)). Minute perturbations in this transverse mode induced by Coriolis forces can be sensitively measured as displacement dy, enabling angular vibration extraction via demodulation of the optomechanical output signal. Quantifying the minimum perceptible mass serves as a means of assessing a gyroscopic sensor's inertial displacement detection limits and therefore its angular vibration resolution [29].

The optical ring resonator is a device that uses the phenomenon of whispering gallery modes (WGM) to confine light in a circular or racetrack-shaped structure [40]. The WGM are optical resonances that occur when the light travels along the circumference of the ring with a total internal reflection condition. The resonance frequency of the WGM depends on the effective refractive index of the ring and the radius of curvature. In the absence of external rotation, the optical power coupled from the waveguide into the integrated optical ring resonator, which establishes the nominal transmission properties of the device, is governed by three coupling mechanisms. The first,

extrinsic coupling (k_e), represents power tunneling between the ring and waveguide via evanescent field overlap and depends on their gap spacing. The second, intrinsic coupling (k_i), accounts for inherent loss pathways within the ring itself. The third component, scattering coupling (k_s), along with the decay rate (k_{tm}) of the test mass (represented by the hemispherical shell), and the losses modeled due to fabrication imperfections at the ring-waveguide interface, are all functions of the gap distance [14], [36]. Furthermore, it should be noted that the coupling of diffusion and the effects of losses due to manufacturing defects were not considered in this model. The reason for this omission is that their impact is relatively minor when compared to the effect of the decay rate of the test mass. Hence, these factors were deemed negligible for the purposes of this analysis.

The working mechanism of the detection by the optical ring resonator can be elucidated by the subsequent mathematical formulations. The ensuing expression dictates the resonant state for the Whispering Gallery Mode (WGM):

$$m\lambda = 2\pi n_{eff} R \quad (10)$$

where m is the azimuthal mode number, λ is the wavelength of light, n_{eff} is the effective refractive index of the ring, and R is the radius of the ring. The optical quality factor of the ring resonator is given by:

$$Q = \frac{\omega}{\Delta\omega} = \frac{\pi n_{eff} R}{\lambda k} \quad (11)$$

where ω is the angular frequency of light, $\Delta\omega$ is the linewidth of the resonance, and k is the total loss rate of the ring, which includes the intrinsic loss k_i, the external coupling loss k_e, and the test-mass induced loss k_{tm}. Furthermore, the output optical field coupled out of the resonator and into the adjoining waveguide satisfies the constraints imposed by the well-established input-output relations. These relations mathematically correlate the external fields at the input/output waveguide ports to the internal dynamics occurring within the ring cavity itself. By describing the interdependence between the optical fields inside and outside the resonator, the input-output formalism provides a theoretical framework for modeling the transmission and dispersion characteristics of the overall integrated optical ring structure [35].

$$T = P_{in} \left| 1 - \frac{k_e}{k_i/2 + k_e/2 + k_{tm}(d_0)/2 + i\Delta} \right|^2 \quad (12)$$

Equation (13) is derived by computing the proportion of the output power to the input power, as specified by:

$$T = \frac{P_{out}}{P_{in}} = \left| \frac{k_e k_i}{k^2/4 + i\Delta} \right|^2 \quad (13)$$

where P_{in} and P_{out} are the input and output power, respectively, and $\Delta = \omega - \omega_0 - W e^{-\alpha d}$ is the detuning of the input light frequency ω from the unperturbed resonance frequency ω_0, which is shifted by $W e^{-\alpha d}$ due to the presence of the test-mass at a distance d from the ring. The parameter α is the decay constant of the evanescent field of the ring. Fig. 6(a) shows the transmission spectrum of the optical ring resonator coupled to the hemispherical shell test mass at different input power based
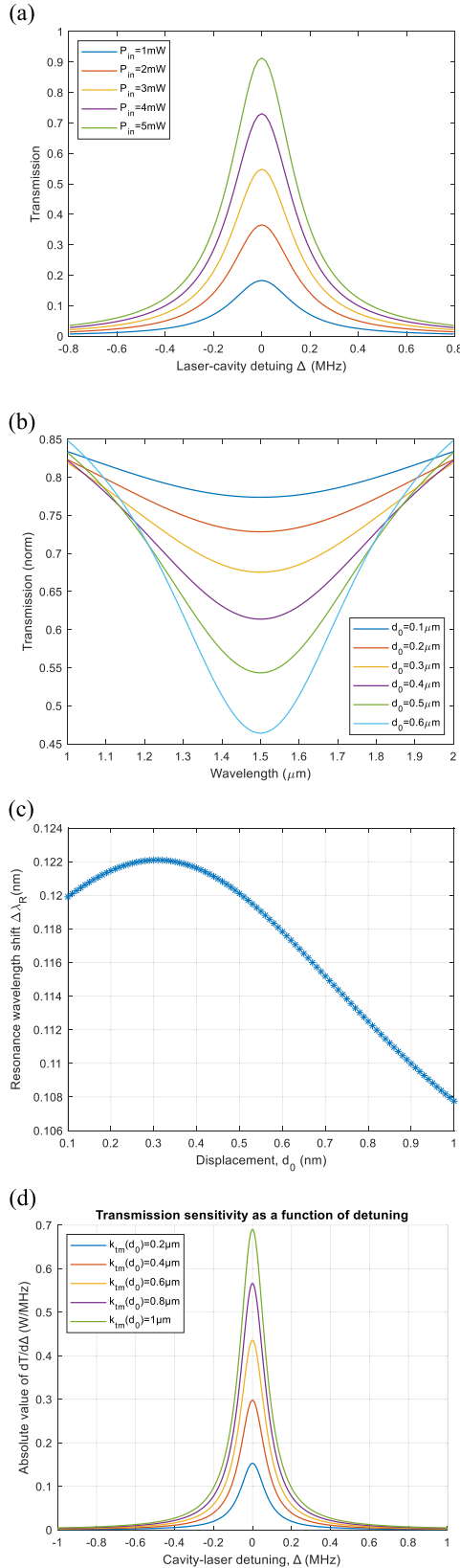
Fig. 6. (a) Influence of input power on WGM mode-changing characteristics. The inset figure illustrates the standard transmission curves for the WGM cavity under various coupling conditions, (b) transmission analysis of a ring resonator coupled to a hemispherical shell test mass at different equilibrium distances, (c) wavelength shifts corresponding to each equilibrium position, and (d) absolute value of $dT/d\Delta$ as a function of in-cavity laser detuning.

on (12) and (13). The optomechanical coupling between the WGM and the test-mass motion is given by:

$$g_{om} = \frac{d\omega}{dx} = \frac{d\omega}{dd}\frac{dd}{dx} = -\alpha W e^{-\alpha d}\cos\theta \qquad (14)$$

where x is the displacement of the test-mass, and θ is the angle between the test-mass motion and the ring plane. The optomechanical coupling rate g_{om} determines the shift of the resonance frequency due to the test-mass motion. Based on (12), we deduce the sensor scale factor, which quantifies the alteration in transmitted power (dT) as a result of the hemispherical shell displacement (dy):

$$\frac{dT}{dy}(d_0) = P_{in}\left| g_{om}(d_0)\frac{\partial T}{\partial \Delta} + \gamma_s(d_0)\frac{\partial T}{\partial k_s} + \gamma_{tm}(d_0)\frac{\partial T}{\partial k_t}\right| \qquad (15)$$

In (15), the dispersive optomechanical coupling rate is represented by $g_{om} = \mathrm{d}\Delta(d_0)/\mathrm{d}d_0$ $g_{om} = \mathrm{d}\Delta(d_0)/\mathrm{d}d_0$, measured in units of Hz/m. The dissipative optomechanical coupling rates are given by $\gamma_s = \mathrm{d}k_s/\mathrm{d}d_0$ $\gamma_s = \mathrm{d}k_s/\mathrm{d}d_0$ and $\gamma_{tm} = \mathrm{d}k_{tm}/\mathrm{d}d_0$ $\gamma_{tm} = \mathrm{d}k_{tm}/\mathrm{d}d_0$, characterizing shifts in the cavity linewidth as a function of equilibrium shell-ring separation d_0. The scale factor defined incorporates both dispersive and dissipative optomechanical effects, with its precise value dependent on the chosen d_0 working point and input laser wavelength $\lambda_L = 2\pi c/\omega_l$. Alternatively, rotational velocities could be deduced from peak shifts in the cavity transmission spectrum away from the intrinsic resonance $\lambda_R = 2\pi c/\omega_0$ incurred by shell vibrations, relying solely on dispersive coupling. In this methodology, the laser is scanned to track resonance motion induced by Coriolis forces on the test mass. Fig. 6(b) shows the wavelength shifts corresponding to each equilibrium position d0. The wavelength shift is proportional to the optomechanical coupling rate g_{om}, which depends on the evanescent field intensity and the effective refractive index of the ring. The figure illustrates how the optomechanical coupling can be tuned by changing the gap distance between the ring and the test mass. An optomechanical coupling factor of $g_{om} = 0.6$ GHz/nm was experimentally determined. Particularly under rate-sensing mode operation, the mechanical dynamics of the oscillating nanomechanical shell gyroscope are governed by the equation of motion [41].

In the stable driving mode that was discussed before, changing the coupling gap d_0 between the micromechanical resonator and optical ring will generate dispersive and/or dissipative modulations, Fig. 6(c) shows the wavelength shifts corresponding to each equilibrium position as a function of the in-cavity laser detuning Δ for different values of d_0. This figure indicates the optimal detuning value for maximizing the sensitivity of the device. As shown in the figure, the optimal detuning value decreases as d_0 increases, which means that the device can operate at a lower laser power and still achieve high sensitivity. Accordingly, by tuning one cavity-laser detuning Δ, any motion changing dy produced in sensing mode would change transmission T, taking dispersive and/or dissipative transduction into account, which may be easily detected by a photoelectric detector (PD), Fig. 6(d) shows the absolute value of $dT/d\Delta$ as a function of the in-cavity laser detuning Δ for different values of d_0.

The scale factor is defined as the ratio of the output optical power change to the input displacement change of the test mass. The scale factor reaches its maximum value when $d_0 = 1 \mu m$, which corresponds to the case of critical coupling between the ring and the waveguide and micro shell. In this case, the transmission T also reaches its minimum value.

Here, it is possible to write the output optical power P_m modulated by mechanical motion in (10) [14], [23], [42].

$$
\begin{aligned}
P_m &= P_{in} \frac{dT}{dy} \eta y(t) \\
&= P_{in} \eta \left| g_{om} \frac{\partial T}{\partial \Delta} + \gamma_s \frac{\partial T}{\partial k_s} + \gamma_{tm} \frac{\partial T}{\partial k_t} \right| y(t)
\end{aligned} \tag{16}
$$

where η represents some realistic losses from the cavity to the detector. And $|a_{in}|^2 = P_{in}/\hbar\omega_l$ [14]. These analytical formulations provide a theoretical basis for relating minute angular motions transduced onto the mechanical shell to detect variations in the integrated photonic cavity's emission spectrum, enabling gyroscopic rotation sensing.

The observation of variations in $\delta y(t)$ as a consequence of alterations in $T(t)$ can be theoretically represented by taking into account both dispersive and dissipative transduction mechanisms [14], [18], [23], given that:

$$
\frac{\partial T}{\partial k_{tm}} = -\frac{4k_e \left(4\Delta^2 + k_e^2 - (k_i + k_{tm})^2 \right)}{(4\Delta^2 + k^2)^2} \tag{17}
$$

$$
\frac{\partial T}{\partial k_e} = -\frac{4(k_i + k_{tm}) \left(4\Delta^2 - k_e^2 + (k_i + k_{tm})^2 \right)}{(4\Delta^2 + k^2)^2} \tag{18}
$$

$$
\frac{\partial T}{\partial \Delta} = -\frac{32k_e(k_i + k_{tm})}{(4\Delta^2 + k^2)^2} \tag{19}
$$

The interplay among these parameters dictates the scale factor at each instance of d_0. A comprehensive discussion of this will be presented in Section III-B.

III. PERFORMANCE CHARACTERIZATION OF OPTOMECHANICAL MHSRG INTEGRATED WITH THE OPTICAL RING RESONATOR

A. Exhibitions of Optical and Mechanical Modes

Simulation studies were conducted in advance of experimental validation as simulations can provide idealized conditions that depart from practical device configurations [41]. To elucidate the interaction terms specified in (1), (2), and (12), a comprehensive analysis and simulation of the optical and mechanical modes of the micro-shell resonator are necessitated, employing Finite Element Method (FEM) modal analysis. Initially, considering that the optical mode of the conventional spherical Whispering Gallery Mode (WGM) cavity is primarily concentrated in the sphere's periphery, the micro hemispherical shell resonator is also capable of forming an optical microcavity with a high optical quality factor. Utilizing the parameters delineated in Table I, the two-dimensional symmetry method is employed to efficaciously simulate the micro-shell resonator in COMSOL. When the excited WGM modes are of the first order (as illustrated in Fig. 1(d)), the optical resonant frequency

TABLE I
OMSRG PARAMETERS USED FOR NUMERICAL FEM COMPUTATION

Symbol	Quantity	Value [a]
R_{shell}	Radius of shell resonator	37 μm
Th	Thickness of shell resonator	1 μm
R_{rod}	Radius of supporting rod	3 μm
h	Height of supporting rod	19.231 μm
R_{or}	Radius of curvature of optical ring resonator	9.61 μm
W_{core}	Core width of optical ring resonator	0.31 μm
$W_{cladding}$	Cladding width of optical ring resonator	3.1 μm
n_{core}	Core refractive index	2.5
M	Effective mass of resonator	273.2 ng
Q_m	Mechanical quality factor	6×10^6
A_g	Angular gain	0.6
ω_m	Mechanical resonance frequency	2π867.71kHz
ω_l	Laser frequency	2π390THz
T_e	Temperature	270
E	Young's module of silica	76700 Mpa
ρ	Density of silica	2500 kg/cm3
μ	Poisson ratio	0.17
n	Refractive index, real part	1.4457
k	Refractive index, imaginary part	1×10^{-10}

is 272.96 THz, and the optical quality factor can attain a value of 6×10^7.

Given that the resonator's form and dimensions significantly influence the optical properties of the cavity [14], the optical resonance frequency and quality factors of WGM are subsequently scrutinized by parameter scanning, contingent on the thickness of the micro hemispherical shell resonator.

The findings, as depicted in Fig. 7(a), reveal that when the thickness of the micro hemispherical shell resonator rises, the resonance frequency and quality factor remain relatively stable. Conversely, when the micro hemispherical shell resonator is excessively thin, the optical resonance frequency escalates, and the optical quality factor diminishes. Fig. 7(b) shows that increasing the radius from 20 μm to 100 μm leads to a decrease in optical resonance frequency and a near-linear rise in quality, which is satisfactory. The quality factor will be improved from around 3.1×10^7 to 3.5×10^8.

The dimensions of the micro hemispherical shell resonator not only influence the optical properties of the cavity but also have a significant impact on the mechanical resonant frequency. Typically, inertial sensors require a lower mechanical frequency to achieve optimal precision in sensing performance, but it is challenging to mitigate losses due to external environmental vibrations. Consequently, the specific mechanical resonance frequency warrants careful consideration. In this study, to evaluate the feasibility of the proposed system and the effect of varying structural sizes on the mechanical resonant frequency, we employ the solid mechanics module in COMSOL to simulate the mechanical wineglass modes of the micro hemispherical shell resonator. During simulations, all parameters outlined in Table I are held constant, with the exception of the resonator dimensions, including thickness and radius.

Vibrational systems, inherently dynamic, hinge critically on two parameters: mass and stiffness. Employing shell theory, one can deduce an equation for the shell's natural frequency, which can be fine-tuned through the shell's density, radius, and
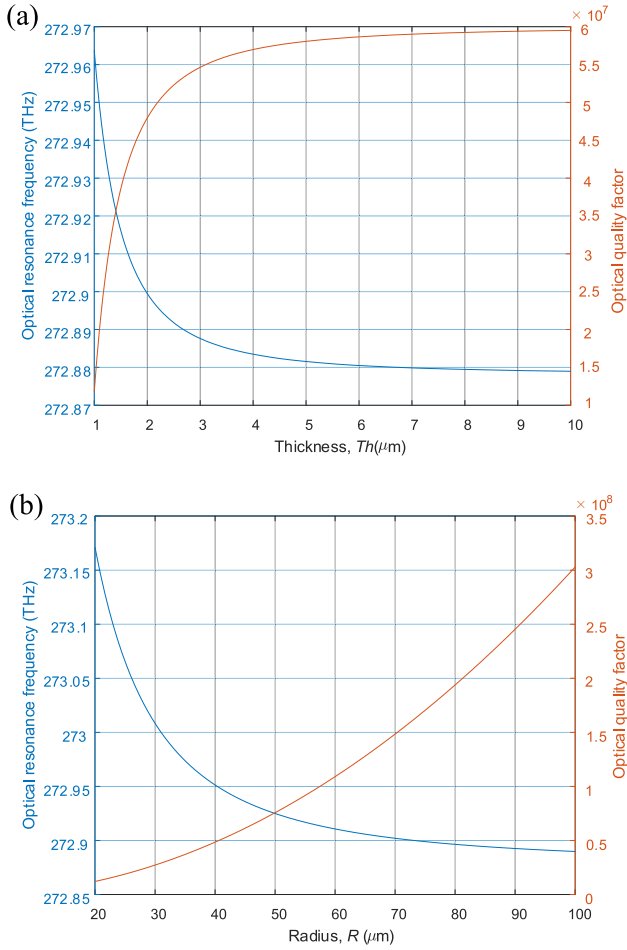
(a)

(b)

(a)

(b)

Fig. 7. Modal analysis of optical and geometrical modes using finite element method (FEM). (a) Variation of optical resonance frequency (blue) and optical quality factors (red) with resonator thickness (Th). (b) Variation of optical resonance frequency (blue) and optical quality factors (red) with resonator radius (R).
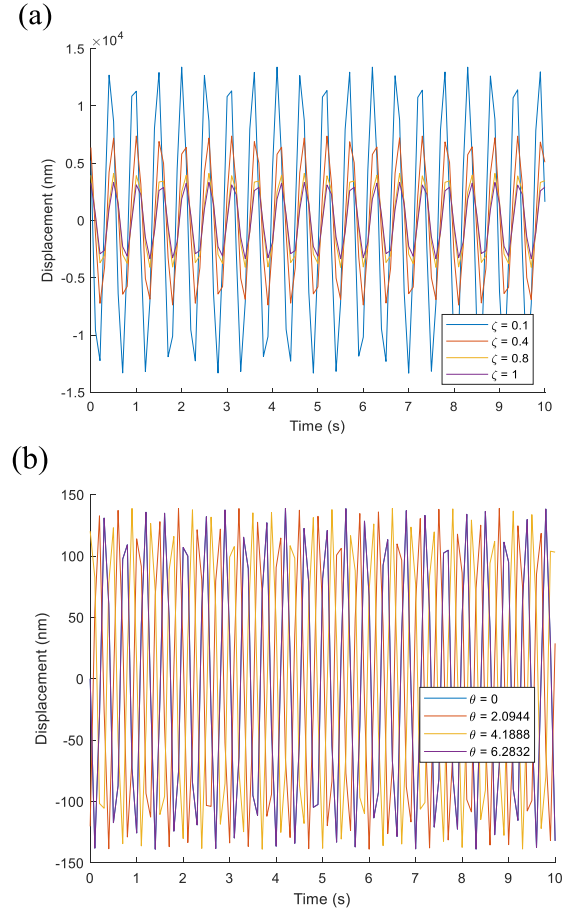
Fig. 8. Forced vibration responses: (a) Displays the specific outcomes of forced vibrations across varying levels of damping. (b) Illustrates the specific outcomes of forced vibrations for a range of phase angles.

thickness to achieve a specific tonal quality. The damping ratio, ascertainable via the logarithmic decrement, offers an approximation of the system's total damping. Given that the hemispherical shell system, with its evenly distributed mass, is subject to forced vibration due to Coriolis forces during rotational vibration, a sinusoidal component emerges, instigating vibration along the rotation angle. The resultant equation of motion parallels that of free vibration but constitutes a non-homogeneous differential equation. Its resolution is a composite of two functions: a complementary solution addressing the homogeneous equation and a particular solution reflecting the impact of external forces.

$$x(t) = Ae^{-ct/(2m)}\sin(\omega_d t + \varphi) + \frac{F_0/k\sin(\omega_f t - \theta)}{\sqrt{(1-r^2)^2 + (2r\zeta)^2}} \tag{20}$$

where ω_f is the external angular vibration frequency, and r is the ratio of the external angular vibration frequency to the driving resonance frequency of the micro-gyroscope. The complementary solution addresses the system's free vibration in an underdamped state, while the particular solution, indicative

of the steady-state response, delineates the system's behavior under continuous external angular vibration. Owing to the micro gyroscopic system's minimal damping, the equation's second term is negligible, leading to significant displacement.

$$x_p(t) = \frac{F_0/k\sin(\omega_f t - \theta)}{\sqrt{(1-r^2)^2 + (2r\zeta)^2}} \tag{21}$$

Illustrating this phenomenon, a plot of normalized maximum displacement against frequency ratio reveals pronounced displacement as the system's angular vibration frequency nears its natural frequency. Based on (21), Fig. 8(a) show the specific outcomes of forced vibrations across varying levels of damping, and Fig. 8(b) show the specific outcomes of forced vibrations for a range of phase angles.

This elucidation aligns with the overarching concept of the scientific paper, which delves into the intricate dynamics of optomechanical gyroscopes. The paper's focus on the micro-hemispherical shell resonator integrated with optical ring cavity resonators underscores the importance of understanding vibrational mechanics to enhance gyroscope performance. The integration of mechanical resonators with photonic elements exemplifies the application of vibrational theory in designing

advanced inertial sensors, thereby contributing to the field's evolution.

B. Performance Characterization of Optomechanical MHSRG

The dispersive and dissipative modulations of the whispering gallery mode for optical ring resonator are highly dependent on the coupling distance between the micro-hemispherical shell resonator and the optical ring resonator with waveguides due to the exponential decay rate of the evanescent field with increasing separation. Accordingly, all the characteristic optomechanical coupling parameters, including the extrinsic coupling rate κ_e, the internal losses κ_i, the external test-mass coupling rate (shell resonator mass) k_{tm}, and the laser-cavity detuning Δ, exhibit an exponential variation with the coupling distance d_0. This exponential relationship between the key optomechanical coupling parameters and d_0 can be attributed to the nature of evanescent coupling, whereby the strength of interaction between the resonator and waveguides decreases sharply following an exponential decay function as the separation increases. Therefore, precisely controlling the coupling distance d_0 allows for optimizing these parameters and maximizing the dispersive and dissipative transduction effects underlying the optomechanical sensing mechanism [23].

In the numerical simulations presented in the paper, the variations of the key optomechanical coupling rates with coupling distance d_0 were modeled based on experimentally measured decay rates. Specifically, the extrinsic coupling rate κ_e was defined as $1.013 \times 10^9 e^{(-8.8 \times 10^{\wedge}-6d0)}$ Hz, the external test-mass coupling rate (shell resonator mass) κ_{tm} was defined as $0.5 \times 10^9 e^{(-8.8 \times 10^{\wedge}-6d0)}$ Hz to characterize intrinsic optical dissipation. Meanwhile, the intrinsic optical decay rate κ_i was fixed at 6×10^6 Hz to account for material absorption within the hemispherical resonator. Additionally, the laser-cavity detuning Δ, representing the offset between the laser and optical ring resonance frequencies, was defined as $0.649 \times 10^9 e^{(-13.8 \times 10^{\wedge}-6d0)}$ Hz. These exponential relationships between the optomechanical coupling parameters and coupling distance d_0 were experimentally verified in previous studies, thereby lending physical validity to the numerical simulations presented in the current work [23].

Based on the aforementioned exponential relationships between the optomechanical coupling parameters and coupling distance d_0, Fig. 9(a) illustrates the resulting variations. The dissipative modulation of the optical ring resonator linewidth is characterized by the damping rates γ_{om}, and γ_t, defined as the derivatives of the extrinsic (κ_e), and test mass (κ_{tm}) decay rates with respect to d_0, or mathematically, $|\gamma_{om}| = d\kappa_e/dd_0$, and test-mass rate $|\gamma_t| = d\kappa_{tm}/dd_0$ is included to represent intrinsic optical losses. Furthermore, the dispersive optomechanical coupling rate g_{om}, describing the shift in the optical ring resonator's optical resonance frequency due to changes in the local effective index of refraction, is given by $g_{om} = d\Delta/dd_0$. Considering only small displacements of the micro-shell resonator around a fixed d_0, these parameters may be linearized as $g_{om} = d\Delta(d_0)/dd_0$, $\gamma_{om} = d\kappa_e(d_0)/dd_0$, and $\gamma_{tm} = d\kappa_{tm}(d_0)/dd_0$, following previous works. As depicted in Fig. 9(b), the magnitudes of these
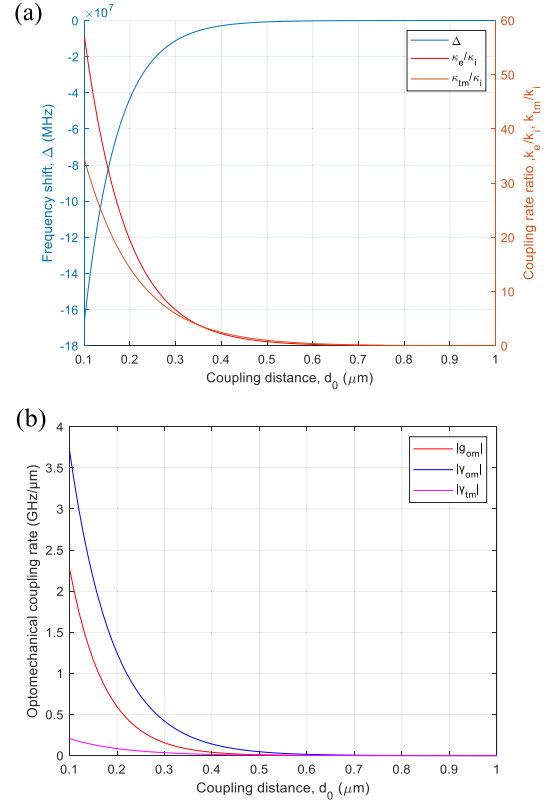

Fig. 9. Theoretical calculation of optomechanical coupling parameters as a function of waveguide-resonator separation distance, (a) resonance frequency shift ($\Delta\omega$) and optical coupling rates (κ_e, κ_i, κ_{tm}) as an exponential function of the separation distance d_0. The intrinsic coupling rate κ_i is determined by the resonator material properties, (b) magnitude of the dispersive (g_{om}) and dissipative (γ_{om}, γ_{tm}) optomechanical coupling rates varying exponentially with the separation distance d_0.

optomechanical coupling rates decrease rapidly with increasing d_0 over short ranges such as $d_0 < 0.2 \ \mu m$, indicating a region of high transduction sensitivity for detecting minor shifts in the coupling gap [18], [43], [44].

These experiments validate the device's capacity to precisely track rotational stimuli through detectable open-loop variations in photo-detected voltage, as well as the influence of scale factor, d_0 gap, and laser power on the transduction slope. The results align well with theoretical predictions, confirming the proposed optomechanical design's viability for high sensitivity rotation sensing applications.

C. Theoretical Analysis of Sensing Sensitivity and Noise Boundaries

This section analyzes the theoretically predicted sensing sensitivity and noise limits of the proposed optomechanical micro hemispherical shell resonator gyroscope (OMHSRG). When operated in rate detection mode, a continuous external driving force is applied to maintain the vibrational driving of the resonator in one direction while the sensing direction displacement is kept at zero. Generally, a higher sensing sensitivity, or scale factor, helps to improve the signal-to-noise ratio (SNR) and reduce bias instability.

In this research, we perform a numerical analysis of the OMHSRG design, focusing on the scale factors of various noise sources mechanical and thermal noise (ARW_{mech}), photodetector noise (ARW_{NEP}), laser shot noise (ARW_{SN}), and back-action noise (ARW_{ba}) to determine their collective impact on the gyroscope's angular random walk (ARW_{total}), which is indicative of its precision and stability in measuring rotational rates.

The scale factors of the proposed high-precision angular rate detection based on an optomechanical micro hemispherical shell resonator gyroscope can be defined as follows: Firstly, the mechanical scale factor (S_{mech}) represents the ratio of the amplitude of displacement (C_y) in the sensing mode to the external input rotation rate (Ω). S_{mech} quantifies the mechanical transduction of the applied rotation rate to a sensed displacement. Secondly, the optomechanical scale factor (S_p) denotes the ratio between the output power (P_m) and C_y. S_p characterizes the transduction of the sensed displacement to a modulated optical output power. Thirdly, the photoelectric conversion scale factor (S_V) is determined by the photodetector (PD) used. Together, these three elements comprise the   overall end-to-end sensitivity of the gyroscope design [14].

$$SF = \frac{V_{out}}{\Omega} = S_{mech} \cdot S_P \cdot S_V \qquad (22)$$

In this study, a U2T BPRV2125A PD is selected, which provides a S_V of 2800 V/W based on its specifications [14]. S_V translates the modulated optical output power to a measurable electrical signal. When the OMHSRG design is perfectly matched to its resonance modes, S_{mech} can be expressed based on (1), and in Appendix A as a function of the system parameters. This represents the theoretical maximum mechanical transduction of the applied rotation rate for the given OMHSRG design parameters under ideal operating conditions.

$$S_{mech} = \frac{C_y}{\Omega_z} = \frac{4A_g F_{drive}}{c_{22}} \qquad (23)$$

By combining the previously defined scale factors, the relationship between the final output voltage (V_{out}) and the input rotation rate (Ω) can be determined. As described in Section II. The optomechanical scale factor (S_p) can be obtained based on (10):

$$S_p = \frac{P_m}{y}$$
$$= P_{in} \frac{dT}{dy} \eta = P_{in} \eta \cdot \left| g_{om} \frac{\partial T}{\partial \Delta} + \gamma_{om} \frac{\partial T}{\partial k_e} + \gamma_{tm} \frac{\partial T}{\partial k_t} \right| \qquad (24)$$

The Angle Random Walk (ARW) is a key metric used to characterize the short-term angular vibration accuracy of the micro hemispherical shell resonator gyroscope (OMHSRG). When operated in a forced balanced mode under perfectly mode-matched conditions, the mechanical Angle Random Walk (ARW_{mech}) can

be expressed as [14], [29]:

$$ARW_{mech} = \frac{1}{2A_g F_{drive}} \sqrt{\frac{k_B T_e}{m \omega_m Q_m}} \cdot \frac{180}{\pi} \cdot 60 \left({}^\circ/\sqrt{h} \right) \qquad (25)$$

where Q_m is the mechanical quality factor, k_B is the Boltzmann constant, and T is the temperature in Kelvin. In addition, the photodetector (PD) introduces electronic noise which can be quantified using the noise-equivalent power (NEP) metric. For the Newport 2117 detector selected, the NEP is specified as 2.8 $pW/Hz^{1/2}$ by the manufacturer. This equation defines the theoretical lower limit of the ARW_{mech} for the OMHSRG.

By relating the output voltage to the input rate through the combined scale factors, the scale factor of the system is determined. In turn, this allows calculation of the ARW_{mech} based on the system parameters to provide a measure of the short-term angular vibration accuracy potentially achievable with the proposed design under ideal forced balanced operation. The NEP represents the optical power that would produce a signal-to-noise ratio of 1 when measuring broadband thermal noise over a 1 Hz bandwidth. Therefore, it provides a measure of the detection noise floor associated with the optical-to-electrical transduction by the specific photodetector.

The optomechanical micro hemispherical shell resonator gyroscope (OMHSRG) measurement noise in terms of equivalent rotation rate can be determined from the detector output noise through the system scale factor (26) shown at the bottom of this page, where P_{det} is the optical power detected and η_{qe} is the quantum efficiency of the detector. For the experimental parameters used, the calculated shot noise power is $\sqrt{2\hbar \omega l P_{det} \eta_{qe}} = 6 \ pW/ \ Hz^{1/2}$. In addition, the shot noise in the optical ring resonator will exert radiation pressure, causing mechanical motion of the resonator, known as back-action noise. This back-action noise can also limit the gyroscope performance. It can be quantified by first determining the back-action noise power spectral density, then converting it to an equivalent rotation rate noise (ARW_{ba}) through the mechanical scale factor (S_{mech}):

$$ARW_{ba} = \frac{\hbar g_{om}}{2m \omega_m A_g F_{drive}} \sqrt{\frac{2n_c}{k}} \frac{180}{\pi} \cdot 60 \left({}^\circ/\sqrt{h} \right) \qquad (27)$$

To determine the overall achievable precision of the micro hemispherical shell resonator gyroscope, it is necessary to account for all noise sources.

The total angular random walk (ARW_{total}) can be expressed as the root sum square of the individual noise contributions:

$$ARW_{total}$$
$$= \sqrt{ARW_{mech}{}^2 + ARW_{NEP}{}^2 + ARW_{SN}{}^2 + ARW_{ba}{}^2} \qquad (28)$$

$$ARW_{NEP} = \frac{NEP}{\left(P_{in}\eta \left| g_{om} \frac{\partial T}{\partial \Delta} + \gamma_{om} \frac{\partial T}{\partial k_e} + \gamma_s \frac{\partial T}{\partial k_s} + \gamma_t \frac{\partial T}{\partial k_t} \right| \right) \cdot S_{mech}} \frac{180}{\pi} \cdot 60 \left({}^\circ/\sqrt{h} \right) \qquad (26)$$

By taking the square root of the summed individual noise terms, the total *ARW* captures the effect of noise propagation in a combined noise model. It represents the expected precision of the gyroscope when all fundamental noise sources are considered. Comparing the calculated ARW_{total} to state-of-the-art systems enables assessment of whether the proposed design can achieve a targeted level of angular random walk performance. Such analysis is necessary to validate theoretical device models against experimental demonstrations.

Based on the presented theoretical calculations, we now analyze the sensitivity and noise limitations of the proposed optomechanical micro-hemispherical shell resonator gyroscope (OMHSRG). Fig. 10(a) illustrates the total scale factor (SF) due to the d_0 dependence for different input powers, Fig. 10(b) illustrates the angle random walk (ARW) decay exponentially with the gap distance (d_0) due to the d_0 dependence of the optomechanical scale factor (Sp).

Additionally, increased frequency splitting ($\Delta\omega$) between the driven (ω_1) and sensed (ω_2) resonant modes results in a reduced mechanical scale factor (S_{mech}) under equivalent excitation due to a lower amplitude detectable displacement. Nevertheless, raising either the input laser power (Fig. 10(c)) or mechanical quality factor (Fig. 10(d)) can counteract the deterioration of sensitivity arising from larger $\Delta\omega$. In summary, analyses are conducted as a function of the design parameters d_0 and $\Delta\omega$, with sensitivity optimized by setting $d_0 = 0.4~\mu m$ and leveraging an adjusted laser power or Q-factor to facilitate maximal gyroscope performance.

In conclusion, the preceding analyses systematically characterized how sensitivity and the work systematically investigated how the optomechanical gyroscope's sensitivity, dynamic measurement range and angular random walk (*ARW*) noise are impacted by variations in key design parameters. Specifically, numerical simulations and analytical modeling were employed to elucidate the influence of tuning the modal frequency splitting ($\Delta\omega$) between driven and sensed vibrational states. The results demonstrated an inherent performance tradeoff between sensitivity and dynamic range that arises from adjustments to $\Delta\omega$. While increased sensitivity is favorable for some applications, others may necessitate an expanded dynamic range to satisfy operational requirements. Critically, the ability to configure $\Delta\omega$ provides a design knob for optimizing the gyroscope architecture depending on the target use case objectives. By navigating the trade-space between sensitivity and dynamic range afforded by selective control of $\Delta\omega$, the proposed optomechanical micro hemispherical shell resonator gyroscope design can be tailored to achieve the balanced competing performance attributes mandated by a given operational environment or mission profile. This work therefore establishes a pathway toward specialized configuration of the gyroscope for applications with differing sensing priorities.

IV. COMPARATIVE STUDY

In this section, we compare the performance of previously reported micro-opto-electro-mechanical systems (MOEMS) gyroscopes to the proposed hemispherical shell resonator
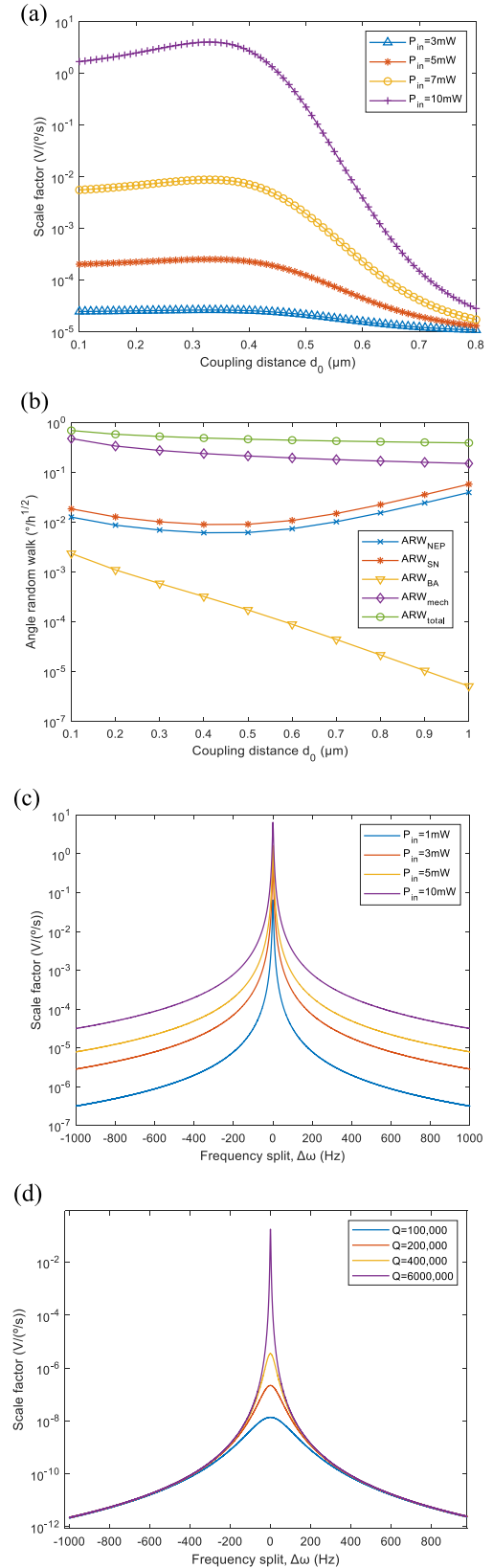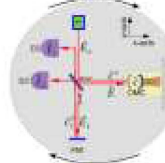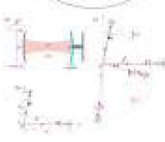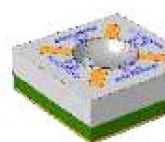

Fig. 10. Numerical simulations of optomechanical performance metrics for a micro hemispherical shell resonator gyroscope (OMHSRG) as a function of structural parameters. Metrics shown include (a) scale factor and (b) angle random walk (ARW) versus coupling distance, and (c) scale factor and (d) ARW versus frequency split. Calculations assume material and dimensional properties of a typical silica OMHSRG as specified in Table I.

TABLE II
COMPARATIVE EVALUATION OF SENSING PERFORMANCE METRICS FOR MICRO-OPTOMECHANICAL SYSTEMS (MOMES) AND OPTOMECHANICAL MICRO HEMISPHERICAL SHELL RESONATOR GYROSCOPE (OMSRG) DESIGNS BASED ON THEORETICAL/NUMERICAL SIMULATIONS

Gyroscope type	Structure	Proof mass	Resonator size [a]	Driving method	Sensitivity	ARW ($°/h^{1/2}$)
Micro Hemispherical Resonator Gyroscope (MHRG) [45]		-	Diameter = 12 mm Height = 4.5 mm Thickness = 200μm	Out-of-plan electrodes	53 mV/(°/s)	0.022
micro-glassblown wineglass resonator [46]		-	5.5 mm × 5.5 mm	Out-of-plan electrodes	0.49 mV/(°/s)	-
Micro Hemispherical Resonator Gyroscope (MHRG) [47]		-	Radius = 275μm Thickness = 50 μm The gap (shell-electrodes) = 5.9μm	Out-of-plan electrodes	-	-
Gyroscope with two-dimensional optomechanical mirror [21]		1.83 mg	Dimensional mirror with a diameter 1 mm and a thickness of 0.5 mm	Optomechanical	10^{-11} rad/s/Hz$^{1/2}$	-
Optomechanical gyroscope [48]		4.77 mg	Dimensional mirror with a diameter 1.5 mm and a thickness of 0.5 mm	Optomechanical	10^{-5} rad/s/Hz$^{1/2}$	-
Optomechanical gyroscope [22]		2.62 mg	Dimensional mirror with a diameter 1.2 mm and a thickness of 0.5 mm	Optomechanical	10^{-9} rad/s/Hz$^{1/2}$	-
OMEMS		212 ng	150 μm × 150μm Radius = 37μm Thickness = 1 μm The gap (shell-electrodes) = 1μm	Out-of-plan electrodes	77.9 mV/(°/s)	0.0662

gyroscope integrated with an optical ring cavity resonator. Existing hemispherical shell resonator gyroscope designs have faced challenges associated with surface metallization and electronic noise [45], [46], [47] (see Table II). Other optical gyroscopes can experience issues achieving perfect coaxial alignment of optical and mechanical axes experimentally [21]. Some designs exhibit limited resolution and bandwidth, resulting from low mechanical quality factors [48]. Additional complexity, susceptibility to lock-in effects, vibration sensitivity, calibration requirements, and constrained detectable angular velocity ranges have been reported, with some designs restricting assumptions to low rotation rates or relying on quadrature phase detection [22]. In contrast, the proposed hemispherical shell resonator gyroscope integrated with an optical ring cavity resonator combines the principles of shell resonators and optical ring cavity resonators. This approach addresses challenges in measuring displacements of the resonant frequency in resonant gyroscopes. Through theoretical analysis, it demonstrates superior performance characteristics, such as the highest simulated sensitivity and lowest noise levels at an input

laser power of 5 mW. Importantly, the design offers the advantages of low cost and extremely miniaturized dimensions for an ultralight test mass. Moreover, the optical detection method is unaffected by electromagnetic interference. Therefore, the novel gyroscope architecture presented here represents a promising solution for next-generation inertial measurement applications by overcoming the limitations of previous approaches.

V. CONCLUSION

In this work, an optomechanical micro-hemispherical shell resonator gyroscope incorporating an integrated optical ring cavity was proposed and numerically investigated to detect rotation rate. The device consists of a micro-hemispherical shell resonator supported on a substrate made with silicon, its deposition with a boron-doped poly-silicon layer, and an optical ring coupled to a waveguide. Finite element simulations elucidated the effects of resonator size on optical and mechanical mode profiles. In the driving configuration, the electrostatic electrodes

provide excitation forces. In detection, optomechanics enhances sensitivity while reducing noise.

For a hemispherical shell mass of 212 ng, gap distance optimization yielded a maximum calculated scale factor of 77.9 mV/(°/s) and a total angle random walk of 0.0662 °/h$^{1/2}$ in force-rebalanced operation at 5 mW input power. Relative to prior designs necessitating metallic coatings, complex fabrication is alleviated without degrading quality factors. Optical detection circumvents electromechanical interference noise issues, improving the signal-to-noise ratio. Overall, numerical results demonstrate that this OMHSRG possesses the potential for high-performance gyroscopic applications through an integrated optomechanical design approach leveraging both optical and mechanical domain interactions. Future work will focus on experimental validation and applications in navigation and inertial sensing.

APPENDIX A

Differential equation of displacement component is established as follows:

$$\left(D + \frac{Nh^2}{12}\right)\frac{\cos 2\theta}{R^2\sin^2\theta}\frac{\partial w}{\partial \theta}$$

$$+ \left(\frac{-12D - Nh^2}{12}\right)\frac{\cos\theta}{R^2\sin\theta}\frac{\partial w}{\partial\theta^2}$$

$$+ \Bigg(D + \mu D + D1 + \frac{Nh^2 + \mu Nh^2}{12}$$

$$+ \frac{N1h^2}{6}\Bigg)\frac{\cos\theta}{R^2\sin^3\theta}\frac{\partial^2 w}{\partial\varphi^2}$$

$$+ \left(-\mu D - D1 - \frac{\mu Nh^2}{12} - \frac{N1h^2}{6}\right)\frac{1}{R^2\sin^2\theta}\frac{\partial^3 w}{\partial\theta\partial\varphi^2}$$

$$+ \left(-D - \frac{Nh^2}{12}\right)\frac{1}{R^2}\frac{\partial^3 w}{\partial\theta^3} = -R^2 X \quad (29)$$

$$\left(D + \mu D + D1 + \frac{Nh^2 + \mu Nh^2}{12} + \frac{N1h^2}{6}\right)\frac{1}{R^2\sin\theta}\frac{\partial w}{\partial\varphi}$$

$$+ \left(-\mu D - D1 - \frac{\mu Nh^2}{12} - \frac{N1h^2}{6}\right)\frac{1}{R^2\sin\theta}\frac{\partial^3 w}{\partial\theta^2\partial\varphi}$$

$$+ \frac{-12D - Nh^2}{12}\frac{\cos\theta}{R^2\sin^2\theta}\frac{\partial^2 w}{\partial\theta\partial\varphi}$$

$$+ \frac{-12D - Nh^2}{12R^2\sin^3\theta}\frac{\partial^3 w}{\partial\varphi^3} = -RY \quad (30)$$

$$\left(\frac{-3D\sin^2\theta - D\cos^2\theta}{\sin^2\theta} + \frac{Nh^2 + \mu Nh^2}{12}\right)\frac{\cos 2\theta}{R^2\sin^2\theta}\frac{\partial w}{\partial\theta}$$

$$+ \left(\frac{D\cos^2\theta}{\sin^2\theta} + \frac{Nh^2 + \mu Nh^2}{12}\right)\frac{1}{R^2}\frac{\partial^2 w}{\partial\theta^2}$$

$$+ \frac{Nh^2 + \mu Nh^2}{6}\frac{w}{R^2}$$

$$+ \left(\frac{-2D - 2\mu D - 2D1}{\sin^2\theta} - \frac{Nh^2 + \mu Nh^2}{12}\right)\frac{1}{R^2\sin^2\theta}\frac{\partial^2 w}{\partial\varphi^2}$$

$$+ \frac{-2D\cos\theta}{R^2\sin^2\theta}\frac{\partial^3 w}{\partial\theta^3} + \frac{2(D1 + \mu D)\cos\theta}{R^2\sin^3\theta}\frac{\partial^3 w}{\partial\theta\partial\varphi^2}$$

$$+ \frac{-D}{R^2}\frac{\partial^4 w}{\partial\theta^4} + \frac{-2(D1 + \mu D)\cos\theta}{R^2\sin^2\theta}\frac{\partial^4 w}{\partial\theta^2\partial\varphi^2}$$

$$+ \frac{-D}{R^2\sin^4\theta}\frac{\partial^4 w}{\partial\varphi^4} = -R^2 Z \quad (31)$$

Where R is the radius of middle surface of hemispherical shell, h is the thickness of shell, E is Young's modulus, μ is Poisson ratio, $N = Eh/(1-\mu^2)$, $N1 = Eh/2(1+\mu)$, $D = Eh^3/12(1-\mu^2)$, $D1 = Eh^3/12(1+\mu)$. X, Y, Z are the projection of load (distributed surface force) in the local coordinate system [36].

APPENDIX B

The mechanical equation of the OMHSRG in the rate-sensing mode.

$$\begin{pmatrix} 1 & 0 \\ 0 & 1 \end{pmatrix}\begin{pmatrix} \ddot{x} \\ \ddot{y} \end{pmatrix} + \begin{pmatrix} c_{11} & c_{12} \\ c_{21} & c_{22} \end{pmatrix}\begin{pmatrix} \dot{x} \\ \dot{y} \end{pmatrix}$$

$$+ \begin{pmatrix} k_{11} & k_{12} \\ k_{21} & k_{22} \end{pmatrix}\begin{pmatrix} x \\ y \end{pmatrix}$$

$$+ \begin{pmatrix} 0 & -4A_g\Omega \\ 4A_g\Omega & 0 \end{pmatrix}\begin{pmatrix} \dot{x} \\ \dot{y} \end{pmatrix} = \begin{pmatrix} V_1/m \\ V_2/m \end{pmatrix} \quad (32)$$

where x, y are the generalized displacements of driving mode and sensing mode, A_g is the angular gain, V_i $(i = 12)$ are the driving voltage of each mode, $c_{i,j}$ $(i, j = 12)$ are damping coefficients and $k_{i,j}$ $(i, j = 12)$ are spring coefficients. The mechanical motion of OMHSRG is affected by the above parameters and those parameters have the following relationship:

$$\begin{cases} k_{11} = \frac{\omega_1^2 + \omega_2^2}{2} + \frac{\omega_1^2 - \omega_2^2}{2}\cos 2\theta_\omega \\ k_{12} = k_{21} = \frac{\omega_1^2 - \omega_2^2}{2}\sin 2\theta_\omega \\ k_{22} = \frac{\omega_1^2 + \omega_2^2}{2} - \frac{\omega_1^2 - \omega_2^2}{2}\cos 2\theta_\omega \end{cases} \quad (33)$$

$$\begin{cases} c_{11} = \left(\frac{\omega_1}{2Q_1} + \frac{\omega_2}{2Q_2}\right) + \left(\frac{\omega_1}{2Q_1} - \frac{\omega_2}{2Q_2}\right)\cos 2\theta_\tau \\ c_{12} = c_{21} = \left(\frac{\omega_1}{2Q_1} - \frac{\omega_2}{2Q_2}\right)\sin 2\theta_\tau \\ c_{22} = \left(\frac{\omega_1}{2Q_1} + \frac{\omega_2}{2Q_2}\right) - \left(\frac{\omega_1}{2Q_1} - \frac{\omega_2}{2Q_2}\right)\cos 2\theta_\tau \end{cases} \quad (34)$$

$$m = \int_V \rho(\phi_{x1}^2 + \phi_{y1}^2 + \phi_{z1}^2)dV = \int_V \rho(\phi_{x2}^2 + \phi_{y2}^2 + \phi_{z2}^2)dV \quad (35)$$

$$A_g = \int_V \rho|\phi_{x1}\phi_{y2}|dV/m \quad (36)$$

where θ_ω is the angular difference between spring coordinate system and main coordinate system, θ_τ is the angular difference between damping coordinate system and main coordinate system, ω_1 is the frequency of driving mode, ω_2 is the frequency of sensing mode, Q_1 and Q_2 are the quality factor of driving and sensing mode, respectively; and ϕ_{xi}, ϕ_{yi} and ϕ_{zi} (i = 1, 2) are the shape function of wineglass modes, ρ is the density [14], [21]. Usually, $Q_1 = Q_2 = Q_m$, $\theta_\omega = \theta_\tau = 0$.

REFERENCES

[1] M. Terrel, M. J. F. Digonnet, and S. Fan, "Performance comparison of slow-light coupled-resonator optical gyroscopes," *Laser Photon. Rev.*, vol. 3, no. 5, pp. 452–465, 2009, doi: 10.1002/lpor.200810052.

[2] Z. Xu, B. Xi, G. Yi, and D. Wang, "A novel model for fully closed-loop system of hemispherical resonator gyroscope under force-to-rebalance mode," *IEEE Trans. Instrum. Meas.*, vol. 69, no. 12, pp. 9918–9930, Dec. 2020, doi: 10.1109/TIM.2020.3005282.

[3] Y. H. Lai et al., "Earth rotation measured by a chip-scale ring laser gyroscope," *Nature Photon.*, vol. 14, no. 6, pp. 345–349, 2020, doi: 10.1038/s41566-020-0588-y.

[4] W. Liang et al., "Resonant microphotonic gyroscope," *Optica*, vol. 4, no. 1, pp. 114–117, 2017, doi: 10.1364/optica.4.000114.

[5] K. Liu et al., "The development of micro-gyroscope technology," *J. Micromechanics Microeng.*, vol. 19, no. 11, 2009, Art. no. 113001, doi: 10.1088/0960-1317/19/11/113001.

[6] Z. Xu, B. Xi, G. Yi, and C. K. Ahn, "High-precision control scheme for hemispherical resonator gyroscopes with application to aerospace navigation systems," *Aerosp. Sci. Technol.*, vol. 119, 2021, Art. no. 107168, doi: 10.1016/j.ast.2021.107168.

[7] D. Senkal, M. J. Ahamed, M. H. A. Ardakani, S. Askari, and A. M. Shkel, "Demonstration of 1 million Q -factor on microglass-blown wineglass resonators with out-of-plane electrostatic transduction," *J. Microelectromech. Syst.*, vol. 24, no. 1, pp. 29–37, Feb. 2015, doi: 10.1109/JMEMS.2014.2365113.

[8] M. H. Asadian, Y. Wang, S. Askari, and A. Shkel, "Controlled capacitive gaps for electrostatic actuation and tuning of 3D fused quartz micro wineglass resonator gyroscope," in *Proc. IEEE Int. Symp. Inertial Sensors Syst.*, 2017, pp. 1–4, doi: 10.1109/ISISS.2017.7935688.

[9] S. Singh, T. Nagourney, J. Y. Cho, A. Darvishian, K. Najafi, and B. Shiari, "Design and fabrication of high-Q birdbath resonator for MEMS gyroscopes," in *Proc. IEEE/ION Position, Location Navigation Symp.*, 2018, pp. 15–19, doi: 10.1109/PLANS.2018.8373358.

[10] T. Nagourney, J. Y. Cho, B. Shiari, A. Darvishian, and K. Najafi, "259 second ring-down time and 4.45 million quality factor in 5.5 kHz fused silica birdbath shell resonator," in *Proc. 19th Int. Conf. Solid-State Sensors, Actuators Microsyst.*, 2017, pp. 790–793.

[11] C. Zhang, A. Cocking, E. Freeman, Z. Liu, and S. Tadigadapa, "On-chip glass microspherical shell whispering gallery mode resonators," *Sci. Rep.*, vol. 7, no. 1, 2017, Art. no. 14965, doi: 10.1038/s41598-017-14049-w.

[12] Z. Hou, X. Wu, D. Xiao, X. Wang, and Z. Chen, "Modal coupling error suppression in micromachined gyroscopes by UV laser trimming," in *Proc. IEEE SENSORS*, 2015, pp. 1–4, doi: 10.1109/ICSENS.2015.7370395.

[13] D. Xiao, D. Yu, X. Zhou, Z. Hou, H. He, and X. Wu, "Frequency tuning of a disk resonator gyroscope via stiffness perturbation," *IEEE Sensors J.*, vol. 17, no. 15, pp. 4725–4734, Aug. 2017, doi: 10.1109/JSEN.2017.2712599.

[14] W. Huang et al., "High-precision angular rate detection based on an optomechanical micro hemispherical shell resonator gyroscope," *Opt. Exp.*, vol. 31, no. 8, pp. 12433–12448, 2023.

[15] A. Sheikhaleh, K. Jafari, and K. Abedi, "Design and analysis of a novel MOEMS gyroscope using an electrostatic comb-drive actuator and an optical sensing system," *IEEE Sensors J.*, vol. 19, no. 1, pp. 144–150, Jan. 2019, doi: 10.1109/JSEN.2018.2875076.

[16] C. Trigona, B. Ando, and S. Baglio, "Fabrication and characterization of an MOEMS gyroscope based on photonic bandgap materials," *IEEE Trans. Instrum. Meas.*, vol. 65, no. 12, pp. 2840–2850, Dec. 2016, doi: 10.1109/TIM.2016.2608078.

[17] D. Xia, B. Zhang, H. Wu, and T. Wu, "Optimization and fabrication of an MOEMS gyroscope based on a WGM resonator," *Sensors*, vol. 20, no. 24, 2020, Art. no. 7264, doi: 10.3390/s20247264.

[18] M. Wu et al., "Dissipative and dispersive optomechanics in a nanocavity torque sensor," *Phys. Rev. X*, vol. 4, no. 2, 2014, Art. no. 021052, doi: 10.1103/PhysRevX.4.021052.

[19] B. B. Li, L. Ou, Y. Lei, and Y. C. Liu, "Cavity optomechanical sensing," *Nanophotonics*, vol. 10, no. 11, pp. 2799–2832, 2021, doi: 10.1515/nanoph-2021-0256.

[20] O. Gerberding, F. G. Cervantes, J. Melcher, J. R. Pratt, and J. M. Taylor, "Optomechanical reference accelerometer," *Metrologia*, vol. 52, no. 5, Sep. 2015, Art. no. 654, doi 10.1088/0026-1394/52/5/654.

[21] S. Davuluri, K. Li, and Y. Li, "Gyroscope with two-dimensional optomechanical mirror," *New J. Phys.*, vol. 19, no. 11, 2017, Art. no. 113004, doi: 10.1088/1367-2630/aa8afb.

[22] G. Li, X.-M. Lu, X. Wang, J. Xin, and X. Li, "Optomechanical gyroscope simultaneously estimating the position of the rotation axis," *J. Opt. Soc. Amer. B*, vol. 39, no. 1, pp. 98–106, 2022, doi: 10.1364/josab.441232.

[23] Y. L. Li and P. F. Barker, "Characterization and testing of a micro-g whispering gallery mode optomechanical accelerometer," *J. Lightw. Technol.*, vol. 36, no. 18, pp. 3919–3926, Sep. 2018, doi: 10.1109/JLT.2018.2853984.

[24] Y. Huang et al., "A chip-scale oscillation-mode optomechanical inertial sensor near the thermodynamical limits," *Laser Photon. Rev.*, vol. 14, no. 5, 2020, Art. no. 1800329, doi: 10.1002/lpor.201800329.

[25] J. Chaste, A. Eichler, J. Moser, G. Ceballos, R. Rurali, and A. Bachtold, "A nanomechanical mass sensor with yoctogram resolution," *Nature Nanotechnol.*, vol. 7, no. 5, pp. 301–304, 2012, doi: 10.1038/nnano.2012.42.

[26] E. Sage et al., "Neutral particle mass spectrometry with nanomechanical systems," *Nature Commun.*, vol. 6, 2015, Art. no. 6482, doi: 10.1038/ncomms7482.

[27] I. Favero and K. Karrai, "Optomechanics of deformable optical cavities," *Nature Photon.*, vol. 3, no. 4, pp. 201–205, 2009, doi: 10.1038/nphoton.2009.42.

[28] M. Aspelmeyer, T. J. Kippenberg, and F. Marquardt, "Cavity optomechanics," *Rev. Modern Phys.*, vol. 86, no. 4, pp. 1391–1452, 2014, doi: 10.1103/RevModPhys.86.1391.

[29] M. Sansa et al., "Optomechanical mass spectrometry," *Nature Commun.*, vol. 11, no. 1, 2020, Art. no. 3781, doi: 10.1038/s41467-020-17592-9.

[30] Q. Zhang, Z. Zhou, Y. Shen, W. Rao, and S. Xiao, "The preparation of polysilicon films on highly boron doped silicon substrates and their effects on Cu out-diffusion," *RSC Adv.*, vol. 14, no. 8, pp. 5207–5215, 2024, doi: 10.1039/d3ra08772g.

[31] X. Han et al., "Bulk boron doping and surface carbon coating enabling fast-charging and stable Si anodes: From thin film to thick Si electrodes," *J. Mater. Chem. A*, vol. 9, no. 6, pp. 3628–3636, 2021, doi: 10.1039/d0ta10282b.

[32] S. Sharbaf Kalaghichi, J. Hoß, R. Zapf-Gottwick, and J. H. Werner, "Laser activation for highly boron-doped passivated contacts," *Solar*, vol. 3, no. 3, pp. 362–381, 2023, doi: 10.3390/solar3030021.

[33] Z. Liu, W. Zhang, F. Cui, J. Tang, and Y. Zhang, "Fabrication and characterisation of microscale hemispherical shell resonator with diamond electrodes on the Si substrate," *Micro Nano Lett.*, vol. 14, no. 6, pp. 674–677, 2019, doi: 10.1049/mnl.2018.5601.

[34] M. M. Torunbalci, S. Dai, A. Bhat, and S. A. Bhave, "Acceleration insensitive hemispherical shell resonators using pop-up rings," in *Proc. IEEE Micro Electro Mech. Syst.*, 2018, pp. 956–959, doi: 10.1109/MEMSYS.2018.8346716.

[35] F. Dell'Olio, T. Tatoli, C. Ciminelli, and M. N. Armenise, "Recent advances in miniaturized optical gyroscopes," *J. Eur. Opt. Soc.*, vol. 9, 2014, Art. no. 14013i, doi: 10.2971/jeos.2014.14013.

[36] Z. Xu, G. Yi, Y. Xie, Z. Wei, and Z. Qi, "Influence of external load on hemispherical resonator gyro feedback control system with state constraints," in *Proc. IECON - 43rd Annu. Conf. IEEE Ind. Electron. Soc.*, 2017, pp. 6217–6222, doi: 10.1109/IECON.2017.8217080.

[37] W. Zhao, H. Yang, F. Liu, Y. Su, and C. Li, "High sensitivity rate-integrating hemispherical resonator gyroscope with dead area compensation for damping asymmetry," *Sci. Rep.*, vol. 11, Jan. 2021, Art. no. 2195, doi: 10.1038/s41598-020-80885-y.

[38] M. A. Basarab, B. S. Lunin, V. A. Matveev, and E. A. Chumankin, "Balancing of hemispherical resonator gyros by chemical etching," *Gyroscopy Navigation*, vol. 6, no. 3, pp. 218–223, 2015, doi: 10.1134/S2075108715030025.

[39] S. Singh, J. K. Woo, G. He, J. Y. Cho, and K. Najafi, "0.0062°/√hr angle random walk and 0.027°/√hr bias instability from a microshell resonator gyroscope with surface electrodes," in *Proc. IEEE 33rd Int. Conf. Micro Electro Mech. Syst.*, 2020, pp. 737–740, doi: 10.1109/MEMS46641.2020.9056391.

[40] Y. Lia Li, "Developing optomechanical inertial sensors," *Appl. Opt.*, vol. 59, no. 22, pp. G167–G174, Aug. 2020, doi: 10.1117/12.2601352.

[41] W. Li et al., "A novel high transduction efficiency micro shell resonator gyroscope with 16 T-shape masses using out-of-plane electrodes," *IEEE Sensors J.*, vol. 19, no. 13, pp. 4820–4828, Jul. 2019, doi: 10.1109/JSEN.2019.2903199.

[42] A. G. Krause, M. Winger, T. D. Blasius, Q. Lin, and O. Painter, "A high-resolution microchip optomechanical accelerometer," *Nature Photon.*, vol. 6, no. 11, pp. 768–772, 2012, doi: 10.1038/nphoton.2012.245.

[43] R. Madugani, Y. Yang, J. M. Ward, V. H. Le, and S. Nic Chormaic, "Optomechanical transduction and characterization of a silica microsphere pendulum via evanescent light," *Appl. Phys. Lett.*, vol. 106, no. 24, 2015, Art. no. 241101, doi: 10.1063/1.4922637.

[44] M. Li, W. H. P. Pernice, and H. X. Tang, "Reactive cavity optical force on microdisk-coupled nanomechanical beam waveguides," *Phys. Rev. Lett.*, vol. 103, no. 22, 2009, Art. no. 223901, doi: 10.1103/Phys-RevLett.103.223901.

[45] Y. Shi et al., "Micro hemispherical resonator gyroscope with teeth-like tines," *IEEE Sensors J.*, vol. 21, no. 12, pp. 13098–13106, Jun. 2021, doi: 10.1109/JSEN.2021.3065818.

[46] D. Senkal, M. J. Ahamed, A. A. Trusov, and A. M. Shkel, "Achieving sub-Hz frequency symmetry in micro-glassblown wineglass resonators," *J. Microelectromech. Syst.*, vol. 23, no. 1, pp. 30–38, Feb. 2014, doi: 10.1109/JMEMS.2013.2286820.

[47] R. Wang, B. Bai, W. Zhang, H. Cao, and J. Liu, "Manufacture of hemispherical shell and surrounding eave-shaped electrodes," *Micromachines*, vol. 12, no. 7, 2021, Art. no. 815, doi: 10.3390/mi12070815.

[48] K. Li, S. Davuluri, and Y. Li, "Improving optomechanical gyroscopes by coherent quantum noise cancellation processing," *Sci. China Phys., Mech. Astron.*, vol. 61, no. 9, 2018, Art. no. 90311, doi: 10.1007/s11433-018-9189-6.